CFA/VISHNO 2016

Imagerie paramétrique : une nouvelle frontière pour l'évaluation non destructive super-résolution?

L. Moreau, E. Larose et R. Brossier
Institut des Sciences de la Terre, ISTerre - Maison des Géosciences, 1381 rue de la Piscine BP 53, 38041 Grenoble Cedex 9, France
ludovic.moreau@ujf-grenoble.fr

In nondestructive evaluation, most ultrasonic imaging methods are based on deterministic approaches where the ultrasound energy is focused in the propagation medium to identify a reflector. Several focusing strategies have been tested, such as time-reversal mirrors, beamforming algorithms, or a combination of both such as the CAPON and MUSIC algorithms. These methods are robust to the noise level. However, they suffer inherent weaknesses that limit the range of possible applications. For example, as sons as the travelling paths of ultrasound cannot be identified accurately, artefacts appear in the images. Typically, this happens when reflections and/or mode conversions occur in the medium. In multiple scattering media, such methods can therefore not be used. Moreover, their imaging resolution is limited to objects which size is of the order of the wavelength. We introduce an imaging method where measured data are reconstructed thanks to a numerical model. The approach consists in describing the medium as an ensemble of elastic and geometric parameters, and to infer these parameters via efficient inversion strategies. This approach allows super-resolution imaging capabilities. Numerical and experimental application are presented, including the imaging of defects with guided waves in plates, and the imaging of cracks in a multiple scattering medium (concrete).

1 Introduction

Nondestructive testing methods (NDT) aim at detecting and characterizing structural defects so as to assess the associated level of danger for the structure. In this matter being able to image and finely identify the geometry of defects is crucial. Ultrasound-based techniques consists in focusing the ultrasonic energy in the medium in order to identify an anomaly. The first generation of transducers had limited focusing capacity because their aperture was fixed geometrically during the conception. The next generation of transducers introduced ultrasonic phased arrays that allowed dynamic focusing of the energy, either in transmission with appropriate time delays on each channel, or in reception with imaging algorithms [1].

Current imaging algorithms generally combine different focusing strategies in both transmission and reception. The majority of these algorithms convert the different phase shifts of the signals into waves travel times, which can be mapped into an echographic image via various beam-forming techniques. The most common examples of such algorithms are delay-and-sum methods in time or frequency domain [1], time-reversal approaches [2], or a combination of both known as super-resolution algorithms such as time-reversal MUSIC imaging [3].

A common feature of these methods is that they all rely on the ability to associate a phase shift in the signal with a travel path in the material. This essential step is not always possible, for example when a propagation time corresponds to several paths: in steel longitudinal waves travel about twice the distance of shear waves in the same time. In that case images contain artefacts that may lead to a wrong interpretation of the defect. It is even worse in multiple scattering media (e.g. concrete) where defects cannot even be detected. Another weakness of such methods is their inability to produce a fine description of the defect geometry in the presence of acoustic shadowing or when parts of the defect scatter significantly more energy than others, which is typical when imaging cracks for example.

Using numerical models to minimize a cost function between actual and synthetic data has been a common imaging strategy in Earth Sciences for the last 30 years, and is known as the Full waveform inversion [4]. However, surprisingly in NDT such methods have remained marginal despite the high computing capacities currently available. The full waveform inversion was first introduced in the context of NDT with bulk waves in 2004 under the name of topological gradient [5]. More recently, it was also applied to ultrasonic guided wave imaging [6]. Because such methods rely on the linearization of the problem, they cannot account for multiple scattering, and their resolution capability is limited to the diffraction limit, *i.e.* the half wavelength. Moreover, as for any gradient descent-like method, prior knowledge about the topology of the medium is required to ensure convergence.

In this paper, the same type of cost function is minimized, but the inversion philosophy is different in the sense that the imaged zone is defined with a set of parameters that are to be inferred. The obvious assumption for this approach to work is that actual data can be modeled faithfully, in which case if the output data of the model fits the measurements, then the parameters of the model describe the physics of the problem adequately, including elastic and geometric properties of the material and/or those of the defects. There are 2 methodological difficulties to this strategy. First, it is necessary to identify the relevant parameters and cost function for the inversion process. Second, efficient forward modeling and inversion procedure are required for acceptable computational times. Through various numerical and experimental examples, we demonstrate that this approach leads to imaging capabilities with unprecedented resolution in both 2D and 3D. Examples include super-resolution imaging of corrosion defects in an elastic waveguide, as well as the reconstruction of cracks in concrete.

2 Model-based imaging procedure

Consider the elastic field resulting from the interaction of an ultrasonic wave with an anomaly, *e.g.* a defect. The configuration is not limited to any particular situation: it may correspond to a guided wave problem, a bulk wave problem, a diffuse wave problem or any other scattering problem. We assume that some relevant data about the scattered field can be identified, such as a measurement of the phase and/or amplitude of the ultrasonic waveforms. We also assume that the physics of the problem can be modeled faithfully, for example via a numerical model. The basis of the approach is to build a cost function based on the error, χ, between actual and synthetic data. Let us introduce $\mathbf{X}$, a variable that contains the parameters in the model.

$$\mathbf{X} = \{p_1, p_2, ..., p_M\}^T, \tag{1}$$

where $p_m \in P_m$, the search space associated with parameter m. M is the number of parameters. For example, since the aim is to produce an image of some inspected domain, the image pixels can be defined as blocks of input param-

eters to the model. M depends on prior knowledge about the problem. For example, assume the geometry of the domain and its elastic constants are known *a priori*, then the defect geometry can be reconstructed by finding the "empty" pixels. Obviously, more complicated configurations will necessitate more model parameters for an adequate representation. Testing all combinations of parameters via a grid search may require a prohibitive number of forward modeling executions (even with efficient models), and the solution would be intractable using current computing technology. Next, we describe 2 inversion strategies adapted to multi-parametric problems: a linear and a Bayesian approach.

2.1 Bayesian inversion method

When the solution to the inverse problem depends on a nonlinear sensitivity kernel, the cost function may contain many local minima. In that case linear inversion methods fail to converge unless prior knowledge of the model allows the inversion to be started with a first guess close to the global minimum. A significant advantage of nonlinear approaches is that convergence is ensured regardless the first guess. They also provide a more accurate estimate of the solution and a quantitative metric to its confidence, the trade-off being a much slower convergence rate. In this section we describe a Bayesian inversion method.

Given a set of measured data, each parameter has its own density probability, $P(\mathbf{X}|data)$, also known as the posterior distribution. If known, the posterior distribution of the model parameters given the data is statistically very valuable for NDT. The mean of the posterior distribution indicates the most likely parameters with regard to those data (*i.e.* those that minimize the error between actual and synthetic data), and the spreading of the posterior distribution indicates a confidence in those parameters. In practice, the posterior distribution is generally too difficult to be estimated directly from the data. However, thanks to Bayes' theorem it is proportional to the probability of the data given some model, known as the likelihood $P(data|\mathbf{X})$. This property is exploited by Markov-Chain Monte Carlo (MCMC) methods to estimate the posterior distribution [7]. MCMC methods are based on stochastic sampling of the parameters space via a random walk that is designed to converge towards the posterior distribution. Each sample is attributed a likelihood based on a likelihood function that accounts for measurement errors in the data. Assuming that experimental data are measured with uncorrelated, random errors that follow a normal distribution, then a likelihood function suitable for most data fitting problems is a zero-mean Gaussian function:

$$P(data|\mathbf{X}) = \exp\left(-\frac{\chi^2(\mathbf{X})}{2\sigma^2}\right). \tag{2}$$

The variance of this Gaussian, σ^2, is determined from an estimate of the measurement error (*e.g.* due to noise level or any other source of uncertainty). A classical error metric for χ is the l_2 norm between actual data and the output of the model.

For the present problem the Metropolis-Hastings algorithm (a simplified version of the MCMC algorithm) is implemented. In practice it is initialized with a solution $\mathbf{X^0} = \{p_1^0, p_2^0, ..., p_{N_i}^0\}^T$, and then iterates via the following steps:
1) Based on the previously accepted solution, $\mathbf{X^{n-1}}$, define a candidate solution $\mathbf{X^{cand}}$ by randomly altering the parameters of $\mathbf{X^{n-1}}$ such that

$$\mathbf{X^{cand}} = \mathbf{X^{n-1}} + f(\Delta\mathbf{X}), \tag{3}$$

where f is a function that randomly samples a candidate in $\Delta\mathbf{X} = \{\Delta p_1, ..., \Delta p_{N_j}\}^T$, the step size in the Markov chain. Δp_i is a fraction of the search space associated with parameter p_i.
2) Use the forward model to evaluate output data associated with the candidate and estimate its likelihood $P(data|\mathbf{X})$ with Eq. (2).
3) If the candidate is more likely than the previous accepted solution, then it is accepted, otherwise it is accepted with probability $\frac{P(data|\mathbf{X^{cand}})}{P(data|\mathbf{X^n})}$: sample a random number α between 0 and 1 from a uniform distribution and accept the candidate if

$$\alpha \leq \min\left[1, \frac{P(data|\mathbf{X^{cand}})}{P(data|\mathbf{X^n})}\right], \tag{4}$$

MCMC methods are know to have a slow convergence rate. In this matter, though, they remain amongst the most efficient methods to deal with multi-dimensional non-linear problems. For the sake of comparison, assuming a 5 dimensions problem, The Metropolis-Hastings algorithm merely requires between 5000 and 10000 iterations to converge, while a brut-force exhaustive search of the parameter space requires to test billions of combinations, thus making the solution intractable. For a more detailed description of the Metropolis-Hastings algorithm and its use for NDT imaging purposes, the reader is invited to refer to [8] and [9].

2.2 Linear least-squares inversion method

When the scattering problem is well constrained, it may be possible to build a cost function with very few local minima, which allows linear approaches to be used for solving the inverse problem. Linear inversion methods are known to have a fast convergence rate provided local minima can be avoided, otherwise convergence is uncertain. The linear problem can be written in a general formulation:

$$\mathbf{d} = \mathbf{mX}, \tag{5}$$

where $\mathbf{d}$ represents the observed data, and $\mathbf{m}$ some model that describes the physics of the problem. If the problem can be linearized, it is possible to build a cost function between the data and the model output such that [11]

$$\chi^2(\mathbf{X}) = ||\mathbf{mX} - \mathbf{d}||_D^2 + ||\mathbf{X} - \mathbf{X^{pr}}||_C^2. \tag{6}$$

Note that this cost function depends on 2 error metrics, namely:
- the l_2 norm between the output of the model, $\mathbf{mX}$, and actual data, $\mathbf{d}$,
- the l_2 norm between prior knowledge, $\mathbf{X^{pr}}$, and the model parameters, $\mathbf{X}$.
Subscripts D and C stand for weighting coefficients $\mathbf{C_D^{-1}}$ and $\mathbf{C_C^{-1}}$, *i.e.* the covariance matrices of the data and the parameters, respectively. The former accounts for measurement errors and thus depends on the quality of experimental data, while the latter corresponds to the error between parameters and prior knowledge. It is possible to tune these matrices so as to select which has more influence on the final solution, for example in the way reported in [10]. On can show that

the posterior distribution of the parameters are linked to the prior distribution via the recursive relationship:

$$\mathbf{X^{n+1}} = \mathbf{X^n} + \left(\mathbf{m^T C_D^{-1} m} + \mathbf{C_X^n}\right)\mathbf{m^T C_D^{-1}}\left(\mathbf{d} - \mathbf{m X^n}\right) \quad (7)$$

where parameters in $\mathbf{X^n}$, estimated at iteration n, are used as prior knowledge to determine the posterior estimation $\mathbf{X^{n+1}}$ until the value of χ reaches a satisfyingly low value.

3 Examples

3.1 Imaging defects in elastic waveguides

This section concerns the imaging of complex, sub-wavelength defects in a plate using Lamb waves. This is a very challenging problem, yet with high stakes in many industrial applications, such as aerospace, pipe and transportation. Difficulties come mainly from the nature of guided wave propagation, which is multimodal and dispersive, thus adding to the difficulty of interpreting signals. Each mode has a specific scattering directivity pattern that depends on many parameters: frequency, defect geometry... Thanks to the completeness of the guided wave basis [12], there is a 1:1 relationship between the geometry of the defect and the directivity of scattered modes amplitude around the defect. Therefore for the inverse problem to be well-posed, the full scattered field of all propagating modes should be measured at least at one frequency. In practice, this is difficult because at least 3 fundamental modes exist in 3D, and also because generally only the back scattered field can be measured. However, this problem can be tackled by multiplying sources and/or frequencies when only part of the scattered field is available for the inversion [8].

The first example is a classical industrial problem, i.e. the characterization of a corrosion defect. An example of such defect is given in figure 2-a, which shows the cartography of its geometry in the form of thickness loss versus position on the plate, which was obtained from a laser scan on a corroded area. The defect has a characteristic dimension of 20 mm. The plate is made of Steel (Young's modulus E = 210 Gpa, Poisson's ratio ν = 0.3), has a thickness of 5 mm and the frequency of inspection is 150 kHz. At this frequency-thickness value, the wavelength of the incident mode, S_0, is 35 mm. Note the typical, sharp corrosion pit on top of a more extended corroded area, which makes this type of defect very difficult to characterize remotely with guided wave inspection. The maximum depth of the defect, which is the most critical parameter, can generally not be determined and on-site interventions for an eventual repair or replacement of the corroded structure are decided with empirical criteria. It is therefore essential to be able to provide an accurate estimate of the maximum depth of the defect.

In this example, the scan of the defect is available but not the corresponding experimental data. These were simulated using the defect geometry as input parameters to an efficient finite element (FE) model [13], and by calculating the associated scattered field. Gaussian white noise was added to the scattered field in order to reproduce actual measurement conditions with a 25 dB signal-to-noise ratio. Modeling is performed in the frequency domain at 150 kHz in a steel plate of thickness 5 mm. The resulting scattering pattern of the 3 propagating modes, $\hat{\mathcal{S}} = \{\hat{S_0}(\theta), S\hat{H}_0(\theta), \hat{A_0}(\theta)\}$, is shown in figure 1. Here θ is the angular coordinate around the defect.

Assuming the full scattering pattern of the 3 modes is available for inversion, the cost function to minimize is defined by

$$\chi^2(\mathbf{X}) = \|\hat{S_0}(\theta) - S_0(\theta)\|^2 + \|S\hat{H}_0(\theta) - SH_0(\theta)\|^2 + \|(\hat{A_0}(\theta) - A_0(\theta)\|^2 \quad (8)$$

where $\mathcal{S} = \{S_0(\theta), A_0(\theta), SH_0(\theta)\}$ denotes the scattering pattern of the 3 fundamental modes in the model. This cost function has many local minima due to the complexity of the guided wave problem. Hence the Bayesian method described in section 2.1 is preferred here. The parameters in variable $\mathbf{X}$ are a set of 20 control points which coordinates, $[X, Y, Z]$, define the test parameters of the inversion procedure. A profile of the candidate defect is then generated with a 2D spline interpolation of the control points over a 54 x 54 pixels map. The pixel size of the map is 1x1 mm^2 so that it matches that in the laser-scans of the defects.

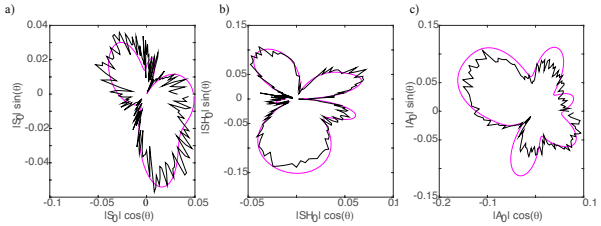

Figure 1: Scattering pattern of the 3 propagating modes: a) S_0, b) SH_0 and c) A_0 when the S_0 mode is incident on the corrosion defect represented in figure 2-a at 150 kHz in a Steel plate of thickness 5 mm. the black line represents simulated experimental data with added white noise of level 25 dB SNR. The pink line is the scattered field from the estimated defect geometry obtained with the Bayesian inversion procedure.

Figure 2-b shows the 3D geometry of the defect estimated from the posterior distribution of the MCMC algorithm. Figure 2-c shows the cross section of the 2 profiles along the [(X=0;Y=0);(X=15;Y=15)] map diagonal, as well as the standard deviation of the solution. There is a very good agreement between the true and estimated defect profiles. The confidence in the solution is also very good. For comparison purpose, conventional imaging with the total focusing method (TFM) is also shown in figure 2-d, where only a spot is visible. In the TFM image the defect geometry cannot be identified and neither can the depth of the defect because this is a 2D image. Interpretation of the image, including the danger associated with the defect, must be made with empirical means. Such difficulties are solved thanks to the Bayesian imaging approach.

In the next example, imaging is applied to experimental data obtained from an approximately circular flat-bottomed cavity manually machined into a 3 mm thick aluminium plate. In order to avoid unwanted reflections from the edges to interact with the scattered wave, the dimensions of the plate are 2mx2m (figure 3-a). The depth of the cavity was measured to range from 0.5 to 1 mm and the diameter was 13 ± 1mm (see photo in figure 3-c).

For data acquisition, Electromagnetic Acoustic Transducers (EMAT) connected to a dedicated amplifier were used and controlled with a Matlab interface. The EMATs are specifically designed for the generation and detection of the S_0

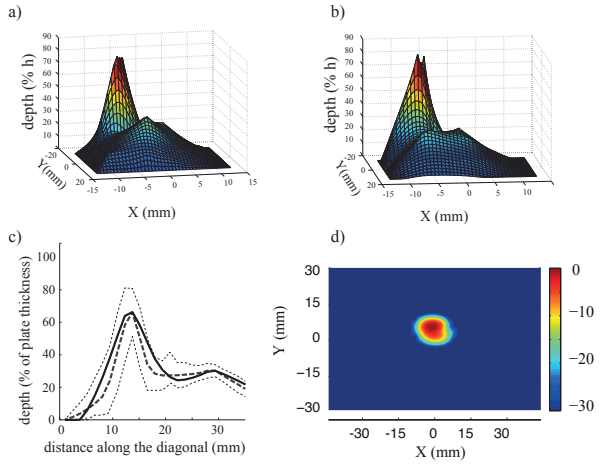

Figure 2: 3D view of a) the true and b) estimated defect with the Bayesian imaging method. c) cross-section of the true (thick solid line) and estimated (thick dashed line) along the [(X=0;Y=0);(X=15;Y=15)] map diagonal, with the standard deviation (light dashed line) d) Conventional imaging using the total focusing method. The colorbar indicates the image dynamic in dB relative to the pixels peak intensity.

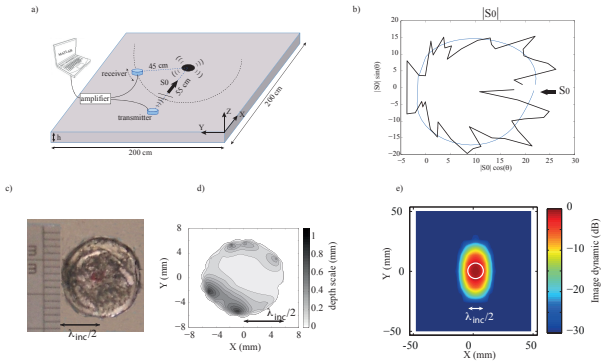

Figure 3: a) Experimental setup of the guided wave experiment in a 3mm aluminium plate; b) Measured scattering pattern for the S_0 mode; c) photography of the defect in the plate; d) estimated defect profile and e) TFM image of the defect.

Lamb mode and exhibit around 30 dB greater sensitivity to this mode than to A_0 and SH_0 modes. It was not possible to measure the amplitude of the other two modes, because appropriate sensors were not available. The transmitted wave is a 3 cycle Gaussian-windowed sinusoidal wave of central frequency 200 kHz. The transmitting EMAT was located 55 cm away from the centre of the defect so that the wavefront of the incident mode can be considered plane. The receiving EMAT was located in the far field of the defect, 45 cm away from its centre, and moved by hand at positions ranging from -110^o to +110^o of the incident direction axis, with an increment of 5^o. The measured signals were then band-passed filtered and Fourier transformed so that the amplitude of the scattered wave could be evaluated at the central frequency. The resulting θ-dependent amplitude of the scattered S_0 Lamb mode has a SNR of 7 dB, and is plotted in figure 3-b.

In the previous example, no prior knowledge was assumed about the defect, because the full scattered fields of the 3 modes were used for inversion. However, only part of the scattered S_0 mode amplitude can be measured in the present case. To compensate for this lack of data, here prior knowledge is assumed about the hole depth, *i.e.* it is less than 2 mm (*i.e.* less than 2/3 of the plate thickness). Because the geometry of the hole is flat-bottomed, contrary to the previous section where the distribution of control points was random, here 20 equally spaced control points are defined on a circle, the radius of which is also a parameter of the inversion process. The Z coordinate of control points is a set of parameter, so that the model may account for depth variations at the contour of the hole. Moreover, to account for the non-perfectly flat bottom, additional control points are considered inside the circle. The estimated profile is shown in figure 3-d. Its diameter is 12.5 mm and its depth varies between 0.2 mm and 1.2 mm. This is consistent with observations made on the true defect and overall the reconstruction of the defect is excellent considering current alternative imaging methods. The scattering pattern from the estimated defect is shown in figure 3-b. For comparison, the TFM image of this defect is plotted in figure 3-e. As expected, since the defect's characteristic dimension is smaller than half the incident wavelength, the TFM reaches the limit of its focusing capability and thus only a large spot is visible. Moreover, as for the previous defect, no information about the depth of the hole is available.

3.2 Imaging defects in multiple scattering media

In this section, we apply the parametric imaging method to multiple scattering media. In a multiple scattering medium, coda waves propagate along complex trajectories, each can be assimilated to a random-walk between scatters. The superposition of coda waves arriving at the sensor is recorded as the coda signal, which temporal waveform is a deterministic representation of the inner structure of the propagation medium. Although coda signals have noisy appearance, they do not fluctuate randomly like noise. Instead, they remain identical unless one or several changes occur in the medium, for instance a reflector or a local change of velocity. The local change(s) modify the propagation trajectory of coda waves, which translates into modifications of the temporal waveform in the coda signals. The severity of the structural change is thus evaluated by its ability of deviating the direction of the acoustic energy, which is quantified with the scattering cross-section γ_e. A large change in the structure scatters more energy, hence results in modifications both in the early and late coda. On the other hand, if the structural change is small, it will scatter little energy and this will not cause significant modifications in the early coda, if any. However, the longer the wave propagates in the medium, the more it interacts with the change, thus accumulating more and more modifications in the coda as compared to the wave that propagates in the medium directly from the source to the receiver. Hence a small change will result in modifications in the late coda [14].

Such changes in the coda wave can be quantified by computing the decorrelation between signals monitored in the medium before and after the change. These will be denoted hereafter by $\phi_0(t)$ and $\phi_1(t)$, respectively. In practice, rather than computing the decorrelation between entire signals $\phi_0(t)$ and $\phi_1(t)$, these signals are first time-windowed into sub-signals of length ΔT, where ΔT is typically of the order of

several mean free times. Estimating the waveform changes at different times in the coda corresponds to probing the medium at different depth, independently. The decorrelation between signals ϕ_0 and ϕ_1 over a time window of length ΔT centered at $t = t_j$ is defined such that:

$$DC^{exp}(t_j) = 1 - \frac{\int_{t_j-\Delta T/2}^{t_j+\Delta T/2} \phi_0(t)\phi_1(t)dt}{\sqrt{\int_{t_j-\Delta T/2}^{t_j+\Delta T/2} \phi_0(t)^2 dt \int_{t_j-\Delta T/2}^{t_j+\Delta T/2} \phi_1(t)^2 dt}}. \quad (9)$$

Consider an experimental setup where N_k source-receiver pairs are used to measure the coda wave in a multiple scattering medium, and let N_j be the number of time windows used to compute the experimental decorrelations. Although current investigations indicate that there might exist an optimal value for the number of time windows N_j and their width ΔT, this is still an on-going research topic. Therefore, next these will be set heuristically to a few mean free times, as suggested in [15], in order to ensure a sufficient number of scattering events in the medium and inversion stability. Hence we introduce the following cost function :

$$\chi(\mathbf{X}) = \frac{1}{N_k} \sum_{k=1}^{N_k} \sqrt{\sum_{j=1}^{N_j} \left(DC_k^{exp}(t_j) - DC_k^{\mathbf{X}}(t_j) \right)^2}. \quad (10)$$

Previous studies showed that the linear inversion can be used to solve the inverse problem [15]. However, the resolution of the mage is limited by the scattering mean free path in that case. In [9] a comparison between the linear and Bayesian inversion methods showed that image resolution can be improved using the MCMC algorithm. Hence in this section, depending on the example either one or the other method (or both) will be considered.

In the first example, experimental data are acquired on the external part of a wind tunnel at ONERA made of concrete, which we instrumented with 16 transmitters and 16 receivers (figure 4-a). The goal was to characterize existing cracks in the structure on the blue area. During aeronautic experiments, pressure is slowly increased inside the wind tunnel, thus also increasing structure stress. This causes the cracks to open. Data were gathered continuously while pressure was building up, by transmitting 2-cycles gaussian-windowed ultrasonic pulses with central frequency 100 kHz. The linear inversion method was applied to decorrelations calculated between signals received at $t_0 = 0$ and $t_1 = 30$ mn.

The forward model used in this inversion is an analytical model based on the radiative transfer equation to calculate the sensitivity kernel of the decorrelations. It allows the calculation of decorrelations induced by a small isotropic change in a multiple scattering medium. A full description of this model can be found in [14]. Here the inverted parameters are the scattering cross-section in each pixel of the image.The reconstructed image is shown in figure 4-b as a density of cracks in m^2/m^3. Images were also calculated in the third dimension and revealed through-thickness cracks, but these are not shown here because no comparison with their actual position is possible (access inside the wind tunnel was not possible). Through-thickness cracks are however consistant with observations made on-site outside the structure where pressurized air was coming out of the cracks. The imaged cracks are in good agreement with the visible part of actual cracks.

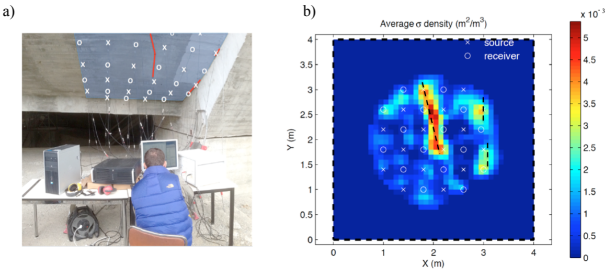

Figure 4: a) Experimental setup at the ONERA site: × indicate transmitters and o indicate receivers. The red line indicates the position of the cracks; b) Result of the linear inversion imaging method, expressed as a density of cracks in $^2/m^3$.

The aim of the last example is to prove via numerical results that cracks can be finely characterized provided the appropriate forward model is used. To this end we consider a multiple scattering medium with elastic properties similar to those of concrete, *i.e.* Young's modulus $E = 35$ GPa and Poisson's ratio $\nu = 0.25$ with a density of 2300 kg/m^3. The model is a 25 mm x 25 mm squared domain, with 100 circular scatterers ($\varnothing$ 10 mm) randomly included. Six sensors acting as both transmitters and receivers are equally spaced on a circle of radius 10 cm centered at the square diagonals. This configuration is shown in figure 5. In order to calculate the decorrelations induced by the appearance of cracks, a 2 cycles tone-burst with a centre frequency of 250 kHz is transmitted in the absence and then in the presence of 3 cracks, which are represented in green in figure 5.

The propagation of signals was then simulated over a 1 ms time window using a commercially available FE software rather than the radiative transfer-based analytical model, which is not designed for extended, anisotropic defects. Decorrelations were subsequently calculated in 5 time windows of 0.2 ms with no overlap, and white noise was added to simulate measurement errors on decorrelations with a SNR of 30 dB. The Bayesian inversion procedure was used to produce an image of the cracks. In this purpose, the parameters to identify are the X and Y coordinates of the cracks center, the cracks orientation, and the cracks dimension. Furthermore, no *a priori* is made about the number of cracks. Consequently, the number of cracks is also a parameter in $\mathbf{X}$. This approach is known as a transdimentional version of the MCMC algorithm [16].

Note that in a classical multiple scattering problem, the location of the scatterers is generally unknown. Therefore, in practice many forward simulations are made, each with a different realization of the disorder that keeps the same transport properties of the medium. The resulting signals are averaged to account for this problem. In the present case, however, this approach would be too time-consuming because parallelization of the simulations is not available. Hence in this last example, it is assumed that the disorder is known but the authors are confident that averaging over several realizations of the disorder would lead to identical results [14]. The mean of the Bayesian posterior distribution is represented in red in figure 5, and very good accuracy is achieved for the 3 cracks.

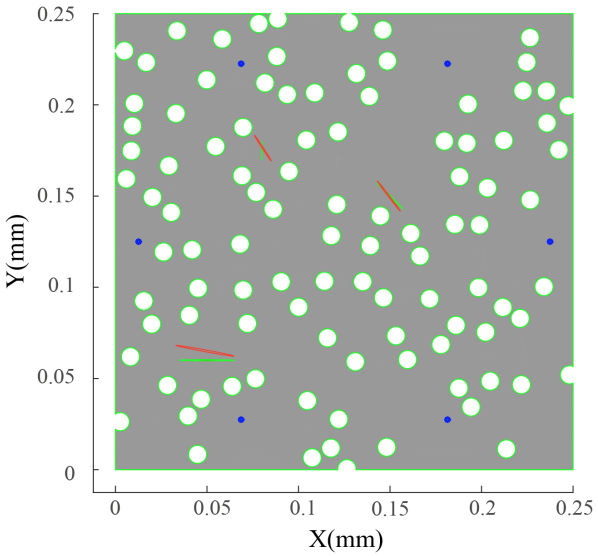

Figure 5: An elastic medium with elastic properties of concrete and 100 scatters of diameter 10 mm. The 3 actual cracks are represented in green and the cracks reconstructed with the Bayesian imaging method are shown in red.

4 Conclusion

This paper introduced a model-based ultrasonic imaging method that aims at minimizing the error between experimental and synthetic data. A cost function is designed and its minimization is achieved via either a Bayesian or a linear inversion method. Once convergence is achieved, the synthetic configuration of the model provides an image of the physical inspected medium. Several numerical and experimental examples were successfully investigated, including remote imaging of corrosion defects with guided waves and the imaging of cracks in multiple scattering media. These results are very encouraging and future developments should focus on the optimization of the inversion procedures, as well as their application to other challenging cases such as the imaging of heterogeneous, anisotropic and attenuative media.

Acknowledgments

This work is funded by the VOR program of the University Grenoble Alpes and is part of the Labex OSUG@2020.

References

[1] C. Holmes, B. W. drinkwater, and P. D. Wilcox, Post-processing of the full matrix of ultrasonic transmit-receive array data for non- destructive evaluation, *NDT&Int.* **38**(8), 701–711 (2005).

[2] N. Chakroun, M. A. Fink and F. Wu, Time Reversal Processing in Ultrasonic Nondestructive Testing, *IEEE Trans. Ultrason., Ferroelect., Freq. Control* **42**(6), 1087–1098 (1995).

[3] Y. Labyed, and L. Huang Ultrasound time-reversal MUSIC imaging with diffraction and attenuation compensation, *IEEE Trans. Ultrason., Ferroelect., Freq. Control* **59**(12), 2186–2200 (2012).

[4] J. Virieux and J. S. Operto An overview of full waveform inversion in exploration geophysics *Geophysics* **74**(6), 127–152 (2009)

[5] N. Dominguez, V. Gibiat, Y. Esquerre Time domain topological gradient and time reversal analogy: an inverse method for ultrasonic target detection, *Wave Motion* **42**(1), 31–52 (2005).

[6] S. Rodriguez, M. Deschamps, M. Castaings and E. Ducasse Guided wave topological imaging of isotropic plates, *Ultrasonics* **54**(7), 1880–1890 (2014).

[7] N. Metropolis, A. W. Rosenbluth, M. N. Rosenbluth, A. H. Teller and E. Teller, Equation of State Calculations by Fast Computing Machines, *J. Chem. Phys* ***21***, 1087–91 (1953)

[8] L. Moreau, A. J. Hunter, A. Velichko and P. D. Wilcox 3-d reconstruction of sub-wavelength scatterers from the measurement of scattered fields in elastic waveguides, *IEEE Trans. Ultrason., Ferroelect., Freq. Control* **61**(11), 1864–1879 (2014).

[9] F. Xie, L. Moreau, Y. Zhang and E. Larose A Bayesian approach for high resolution imaging of small changes in multiple scattering media, *Ultrasonics* **64**(1), 106–114 (2016).

[10] A. Obermann, B. Froment, M. Campillo, E. Larose, T. Planes, B. Valette, J. H. Chen and Q. Y. Liu Seismic noise correlations to image structural and mechanical changes associated with the Mw 7.9 2008 Wenchuan earthquake, *J. Geophys. Res. B: Solid Earth* **119**(4), 3155–3168 (2014).

[11] A. Tarantola, B. Valette, Generalized nonlinear inverse problems solved using the least squares criterion, *Rev. Geophys.* **20**, 219?232 (1982).

[12] P. Kirrmann, On the completeness of Lamb Waves, *J. Elast.* **37**(1), 39–69 (1995)

[13] A. Velichko and P. D. Wilcox, A generalized approach for efficient finite element modeling of elastodynamic scattering in two and three dimensions, *J. Acoust. Soc. Am.* **128**(3), 1004–14 (2010)

[14] T. Planes, E. Larose, L. Margerin, V. Rossetto, C. Sens-Schönfelder, Decorrelation and phase-shift of coda waves induced by local changes: multiple scattering approach and numerical validation, *Wave. Random. Complex*, **24**(1), 99–109 (2014).

[15] E. Larose, T. Planes, V. Rossetto and L. Margerin, Locating a small change in a multiple scattering environment, *Appl. Phys. Lett.* **96**, 204101 (2010)

[16] D. Lamnisos, J. E. Griffin and M. F. J. Steel, Transdimensional Sampling Algorithms for Bayesian Variable Selection in Classification Problems With Many More Variables Than Observations, *Journal of Computational and Graphical Statistics* , **18**(3), 592–612 (2009).